

Cite this: *J. Mater. Chem. A*, 2023, 11, 8256

# Hot carrier relaxation dynamics in non-stoichiometric CdSe quantum dots: computational insights†

Shriya Gumber,<sup>a</sup> Omolola Eniodunmo,<sup>bg</sup> Sergei A. Ivanov,<sup>c</sup> Svetlana Kilina,<sup>b</sup> Oleg V. Prezhdo,<sup>ad</sup> Dibyajyoti Ghosh<sup>ef</sup> and Sergei Tretiak<sup>\*cg</sup>

Spatial confinement of charge carriers in nanosize semiconductor quantum dots (QDs) results in highly tunable, size-dependent optoelectronic properties that can be utilized in various commercial applications. Although in such nanostructures, non-stoichiometry is frequently encountered using conventional synthesis techniques, it is not often addressed or considered. Here, we perform *ab initio* molecular dynamics simulations on non-stoichiometric CdSe clusters to study the phonon-mediated charge carrier relaxation dynamics. We model cation-rich and anion-rich QDs passivated with monocharged neutralizing ligands of different sizes. Our studies confirm the presence of localized trap states at the valence band edge in only anion-rich QDs due to the presence of undercoordinated exposed surface Se atoms. Noteworthy, these localized states disappear when using bulkier ligands. Calculations reveal that the size of the ligands controls the crystal vibrations and electron-phonon coupling, while ligand coordination number affects the electronic structure. For a particular non-stoichiometric CdSe QD, a change of a ligand can either increase or decrease the total electron relaxation time compared to that of stoichiometric QDs. Our results emphasize the importance of ligand engineering in non-stoichiometric QDs for photoinduced dynamics and guide future work for the implementation of improved materials for optoelectronic devices.

Received 9th January 2023  
Accepted 15th March 2023

DOI: 10.1039/d3ta00149k

rsc.li/materials-a

## Introduction

Quantum dots (QDs) are semiconductor nanostructures with all three linear dimensions smaller than or comparable to the exciton Bohr radius. Spatial confinement of charge carriers in these clusters gives rise to size-tunable optical and electronic properties, making them promising materials for a broad range of applications ranging from optoelectronic devices such as light-emitting diodes (LEDs), photovoltaics, and photocatalysis, to biological imaging probes, and quantum computing.<sup>1–5</sup> Due

to the large surface-to-volume ratio, QD properties are highly sensitive to surface morphology and composition. Their photophysical properties can be precisely tuned by modification of the surface, size, ligand passivation, and overall chemical environment.<sup>6–11</sup> The major challenge lies in fabricating identical nanostructures with well-defined shapes and sizes at a large scale. The reproducibility of properties of each unit with the same physical and chemical properties from batch to batch is determined by the complete control of reaction conditions and several parameters, which is hard to maintain in traditional synthesis routes.<sup>12</sup> The chemical composition and geometry of synthesized QDs often differ from the ideal stoichiometric structures. Hence, it is of utmost importance to study how the non-stoichiometry in QDs affects their photophysics and photoexcited dynamics. The phonon-mediated exciton relaxation is essential for both the fundamental understanding and the applications standpoint of QDs since it competes with processes of charge transfer, carrier multiplication, and radiative recombination – key processes that govern the efficiency of both solar-to-electrical and solar-to-chemical energy conversion.<sup>13,14</sup>

The non-stoichiometry in CdSe arises when the cation-to-anion ratio deviates from unity, and it can be realized in two ways: *via* an excess of cations or anions on a QD surface. The coordination sphere of surface ions is not completed by the

<sup>a</sup>Department of Chemistry, University of Southern California, Los Angeles, California 90089, USA<sup>b</sup>Dept. Chemistry and Biochemistry, North Dakota State University, Fargo, North Dakota 58108, USA<sup>c</sup>Center for Integrated Nanotechnologies, Los Alamos National Laboratory, Los Alamos, NM, 87545, USA. E-mail: serg@lanl.gov<sup>d</sup>Department of Physics and Astronomy, University of Southern California, Los Angeles, California 90089, USA<sup>e</sup>Department of Chemistry, Indian Institute of Technology, Delhi, Hauz Khas, New Delhi-110016, India. E-mail: dibyajyoti@iitd.ac.in<sup>f</sup>Department of Materials Science and Engineering (DMSE), Indian Institute of Technology, Delhi, Hauz Khas, New Delhi-110016, India<sup>g</sup>Theoretical Division, Los Alamos National Laboratory, Los Alamos, NM, 87545, USA† Electronic supplementary information (ESI) available. See DOI: <https://doi.org/10.1039/d3ta00149k>

material's counterions, resulting in so-called dangling bonds (unsaturated valences) and localized surface states.<sup>15–19</sup> Often, the charge-neutralizing ligands coordinate with the surface atoms and partially remedy the undercoordination of the latter. Although these nanostructures are common during chemical synthesis, research on these clusters is limited.<sup>20,21</sup> Xia *et al.* reported that the exposed Cd atoms on surface-ligand-removed Cd-rich QDs act as photocatalysts for the conversion of CO<sub>2</sub> to CO.<sup>22</sup> Huang *et al.* manipulated the surface stoichiometry of CdSe QDs by decreasing the amount of surface Se to enhance the photogenerated H<sub>2</sub> evolution yield.<sup>23</sup> Apart from the photocatalytic studies, recently Bhati *et al.* reported the electronic transitions in non-stoichiometric QDs, studied *via* first-principle simulations.<sup>24</sup> However, none of these reports focus on the time-resolved photoexcited charge carrier dynamics. Furthermore, the influence of the size of coordinated ligands on carrier relaxation is yet to be understood at the atomistic level. In this study, we emphasize the importance of a ligand choice to modify the electronic structure, and hence the electron and hole relaxation dynamics for the targeted applications.

The absorption of high-energy photons in molecular and bulk semiconductor materials creates electron–hole pairs or excitons. These hot charge carriers cool to the band edges by losing their energy to vibrations on a femtosecond to a picosecond time scale, predominantly by electron–phonon interactions.<sup>25–27</sup> In QDs, due to the spatial confinement of charge carriers, the electronic states near the band edges are quantized and transitions acquire atom-like discreteness in contrast to continuous broad-band spectra in bulk semiconductors. The energy gap between consecutive orbitals can be larger than the highest phonon frequency of the lattice, leading to an energy mismatch between electronic and vibrational quanta. In turn, it weakens the electron–phonon coupling and substantially slows down the electron and hole cooling dynamics. This phenomenon in low-dimensional materials is known as “phonon bottleneck”.<sup>28–31</sup> In recent decades, alternative relaxation channels such as electron–hole interactions through the Coulomb interaction have been reported that break the phonon bottleneck and lead to faster dynamics, but the ambiguity around it remains unresolved.<sup>32–35</sup> If these proposed alternative channels are suppressed, energy relaxation would be as slow as a few nanoseconds.<sup>35</sup> The suppressed dynamics of excited electrons is favorable for photocatalysis and other relevant applications in QDs.<sup>36</sup> Moreover, slow cooling can result in a higher probability of carrier multiplication (CM): that is, the generation of multiple excitons per photon.<sup>37–39</sup> In this regard, chemical non-stoichiometry can also substantially alter the relaxation dynamics rates of QDs.

Here, we investigate the hot carrier cooling in non-stoichiometric CdSe QDs that are charge-balanced by different-size ligands. As ligands, we utilize cationic H<sup>+</sup>, Na<sup>+</sup>, and K<sup>+</sup> to compensate for the excess of the negative charge in QDs with Cd-to-Se ratio below unity, and anionic halogenides (F<sup>−</sup> and Cl<sup>−</sup>) for positive charge compensation in QDs with the ratio above unity. We employ a mixed quantum-classical approach that includes time-domain density functional theory (TD-DFT)<sup>40</sup> in conjunction with non-adiabatic molecular

dynamics (NAMD)<sup>41</sup> to address how the non-stoichiometry in a quantum dot affects the intra-band electron–phonon relaxation of photogenerated excitons. The atomistic simulation results are followed by *ab initio* molecular dynamics (AIMD) and NAMD calculations to model the photoinduced electron and hole relaxation dynamics. Our results corroborate the literature reports about the presence of localized trap states close to the valence-band edge in only Se-rich clusters.<sup>42</sup> Interestingly, we observe that these states disappear when using bulkier ligands for QD passivation, highlighting the importance of ligand choice in non-stoichiometric QDs. Furthermore, we find that the ligands control lattice vibrations that influence the electron–phonon coupling. This coupling directly affects the rates of phonon-mediated exciton dynamics. With the same Cd/Se configuration, enhanced and reduced electron relaxation rates with respect to their stoichiometric counterparts are obtained by using different ligands. Overall, these atomistic simulations offer the first step towards a comprehensive understanding of how photophysical processes can be tuned by the structural modification affecting the electronic character of QDs.

## Results and discussion

We model (see Computational methods) stoichiometric Cd<sub>33</sub>Se<sub>33</sub> QD (Fig. 1a) (as a reference) together with five non-stoichiometric CdSe systems – two Cd-rich Cd<sub>28</sub>Se<sub>17</sub>X<sub>22</sub> (X = F, Cl) (Fig. 1b and c) and three Se-rich Cd<sub>17</sub>Se<sub>28</sub>M<sub>22</sub> (M = H, Na, K) quantum dots (Fig. 1d–f). The initial Cd<sub>33</sub>Se<sub>33</sub> structure is constructed from the CdSe bulk wurtzite lattice, and it attained the relaxed geometry at the energy minimum upon optimization. Non-stoichiometric QDs, on the other hand, maintain a T<sub>d</sub> symmetry where the Cd and Se atoms are arranged in a hybrid wurtzite/zinc blende crystal structure – the interior of the cluster has the zinc blende atomic arrangement, and the vertices of the tetrahedron have a wurtzite configuration of Cd and Se. Two types of non-stoichiometric QDs can be obtained from each structure by switching the Cd and Se atoms. The excess charge on its surface is balanced by the monocationic H<sup>+</sup>, Na<sup>+</sup> and K<sup>+</sup> in Se-rich QDs – these ligands coordinate to the anionic Se atoms – and by anionic F<sup>−</sup>, Cl<sup>−</sup> ligands in Cd-rich QDs – these ligands coordinate with the cationic Cd atoms. The C<sub>6</sub>H<sub>5</sub>– moiety present in experimental structures is replaced by H<sup>+</sup> for the computational speed up in Cd<sub>17</sub>Se<sub>28</sub>H<sub>22</sub>.<sup>43</sup> The bulkier ligands Na<sup>+</sup> and K<sup>+</sup> replace H<sup>+</sup> in Se-rich QDs to understand the effect of the extent of Se passivation on surface trap states. The values of the average charge on the core, surface, and ligand atoms for all nanoclusters are reported in Table S4.†

Because of the large surface-to-volume ratio, atoms at the core of the QD are in a different chemical environment than those at the surface. In a stoichiometric Cd<sub>33</sub>Se<sub>33</sub> nanocrystal, the core Cd (or Se) is coordinated with four other atoms, while the atoms on the surface are only three-coordinate. Consequently, the Cd–Se bonds on the surface are stronger and shorter compared to the weaker and longer core Cd–Se bonds (Table 1), which agrees with previous calculations.<sup>7</sup> In non-stoichiometric QDs, the monocharged ligands adjust to the surface undercoordination to a different extent, depending on



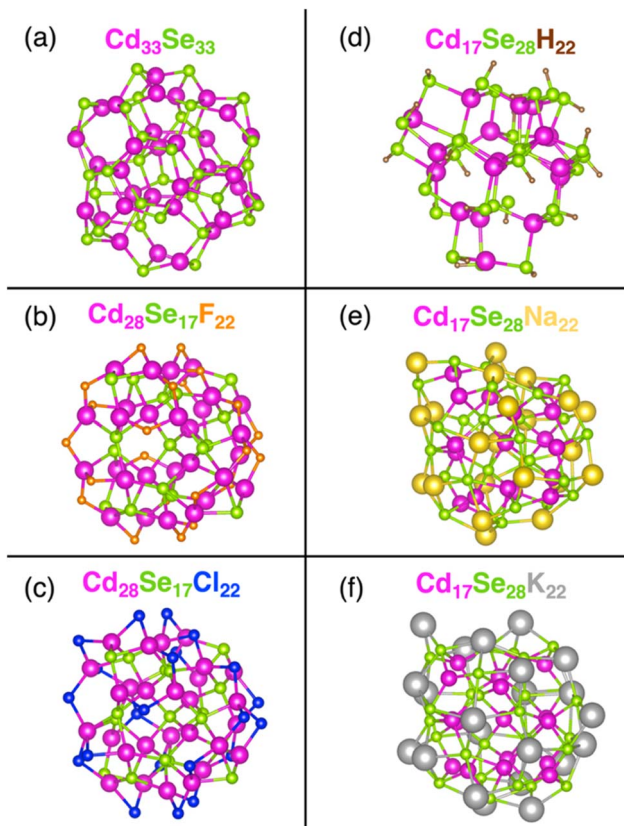


Fig. 1 The DFT optimized geometry of stoichiometric (a)  $\text{Cd}_{33}\text{Se}_{33}$ , and non-stoichiometric: Cd-rich (b)  $\text{Cd}_{28}\text{Se}_{17}\text{F}_{22}$ , (c)  $\text{Cd}_{28}\text{Se}_{17}\text{Cl}_{22}$  and Se-rich (d)  $\text{Cd}_{17}\text{Se}_{28}\text{H}_{22}$ , (e)  $\text{Cd}_{17}\text{Se}_{28}\text{Na}_{22}$ , (f)  $\text{Cd}_{17}\text{Se}_{28}\text{K}_{22}$  quantum dots (QDs). Anionic ligands bond to the surface Cd atoms and cationic ligands bind to the surface Se atoms. Each  $\text{H}^+$  is monodentate *i.e.*, it coordinates only one Se atom per ligand and leads to the formation of a polar covalent H–Se bond. The denticity of other ligands ranges from two in Cd-rich QDs to two to four in Se-rich QDs, due to the more ionic interaction.

their size. In Se-rich QDs, the H atom binds to only one surface Se atom due to the small size of the former, formally giving rise to a commonly encountered hydroselenide anion,  $\text{HSe}^-$ . Furthermore, only 22 ligands in  $\text{Cd}_{17}\text{Se}_{28}\text{H}_{22}$  are available for 24 surface Se atoms, leaving two surface Se atoms not bonded to a ligand. This ligand arrangement further increases the difference between the surface and core Cd–Se bond lengths.  $\text{Na}^+$  and  $\text{K}^+$ , on the other hand, have larger surface coordination

numbers, thus leading to a decreased difference between bond lengths of two types of Cd–Se bonds. In Cd-rich QDs, following a similar trend, the halogenide coordination results in a little (in the case of  $\text{F}^-$ ) to none (in the case of  $\text{Cl}^-$ ) bond length difference between interior and surface Cd–Se bonds.

Fig. 2 shows the projected density of states (PDOS) derived by the projection of the total density of states into atomic orbitals for optimized geometries at 0 K of all systems under investigation. Insets show the charge density plots of the Kohn–Sham (KS) orbitals corresponding to the highest occupied molecular orbital (HOMO) and lowest unoccupied molecular orbital (LUMO) energies. The LUMO orbital is isolated in energy from the rest of the band, while its charge density is distributed nearly uniformly over the QD for all structures. According to the effective mass approximation, this peak is attributed to the S-electron state emerging from the s-type atomic orbitals of Se.<sup>44</sup> The valence band (VB) state structure is quasi-continuous and is mostly localized on the Se atomic orbitals. In Se-rich QDs, the orbital overlap between consecutive orbitals further increases as the energy gap between those narrows. Because of the deficiency of Se in Cd-rich QDs, the interorbital energy gaps in VB widen thereby increasing the *discreteness* of the VB. The conduction band (CB) is discrete near the band-edge at low energy as expected for the spatially confined nanostructures. The extent of discreteness is subject to the size and ligand coordination. A smaller ligand  $\text{H}^+$  in Se-rich QDs leads to a larger energy difference between the S-electron state and the next higher energy state. These trends in sub-band gaps persist during dynamic processes (Fig. S4 and S5<sup>†</sup>) and play a significant role in electron and hole relaxation rates as discussed later. The  $\text{Na}^+$  or  $\text{K}^+$  cation draws to itself highly polarizable electron density of surface Se anions; in contrast,  $\text{F}^-$  or  $\text{Cl}^-$  anion cannot provide much electron density to many neighboring cationic Cd on the QD surface. Consequently, the surface charges have higher absolute value in Se-rich QDs than in Cd-rich QDs (Table S4<sup>†</sup>). Furthermore, there is an emergence of sub-band gaps in CB of Na- and K-ligated systems, which are more prominent in the K-ligated system. Simulations neglecting the dielectric environment effect tend to generate these in-gap states.

The first three orbitals at the VB edge of H- and Na-ligated clusters appear highly localized. As seen in the charge density plots for the first two orbitals given in Fig. S6,<sup>†</sup> they are mostly localized on the undercoordinated surface Se atoms. However, when a bulkier  $\text{K}^+$  is used in the same configuration of Cd/Se

Table 1 The Cd–Se and Cd(Se)–ligand bond lengths in the optimized structures. The Cd–Se bond lengths differ for the core and surface atoms and are hence shown separately. The  $\text{F}^-$  and  $\text{Cl}^-$  ligands bond only to the surface Cd atoms, while  $\text{H}^+$ ,  $\text{Na}^+$  and  $\text{K}^+$  only bind to the surface Se atoms

Distance (Å)	Cd rich			Se rich		
	$\text{Cd}_{33}\text{Se}_{33}$	$\text{Cd}_{28}\text{Se}_{17}\text{F}_{22}$	$\text{Cd}_{28}\text{Se}_{17}\text{Cl}_{22}$	$\text{Cd}_{17}\text{Se}_{28}\text{H}_{22}$	$\text{Cd}_{17}\text{Se}_{28}\text{Na}_{22}$	$\text{Cd}_{17}\text{Se}_{28}\text{K}_{22}$
Cd–Se surface	2.66	2.67	2.68	2.68	2.70	2.71
Cd–Se core	2.74	2.70	2.68	2.82	2.75	2.76
Se–ligand	—	—	—	1.49	2.93	3.21
Cd–ligand	—	2.21	2.60	—	—	—



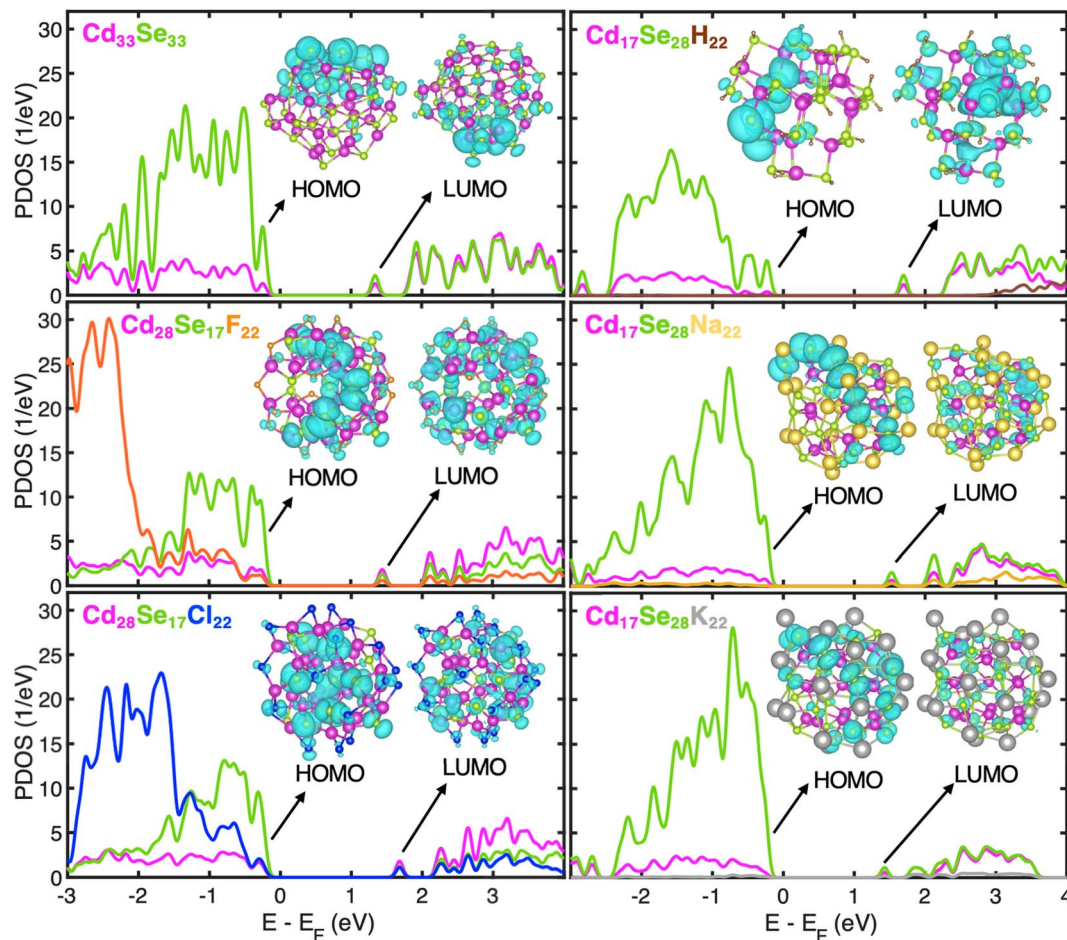


Fig. 2 Projected density of states (PDOS) of stoichiometric,  $\text{Cd}_{33}\text{Se}_{33}$  and non-stoichiometric-Cd-rich  $\text{Cd}_{28}\text{Se}_{17}\text{X}_{22}$ , ( $\text{X} = \text{F}, \text{Cl}$ ) and Se-rich  $\text{Cd}_{17}\text{Se}_{28}\text{M}_{22}$ , ( $\text{M} = \text{H}, \text{Na}, \text{K}$ ) clusters separated into contributions from atomic orbitals for optimized geometries at 0 K. The Fermi energy ( $E_F$ ) level is set to 0 eV. Atom types in the structure, the corresponding PDOS plot, and atomic symbols are represented by the same colour in the upper left corner of each panel. The charge density plots of HOMO and LUMO calculated at an isosurface level of  $0.0005e a_0^{-3}$  (where  $a_0$  is the Bohr radius) are in turquoise colors in the insets for each system. The LUMO is separated from the rest of the conduction band by an energy gap greater than 0.4 eV.

atoms, this localization disappears. Because of its larger size, it is easier for  $\text{K}^+$  to extend bonding to the undercoordinated Se compared to  $\text{H}^+$  and  $\text{Na}^+$ . Consequently, HOMO and HOMO-1 of  $\text{Cd}_{17}\text{Se}_{28}\text{K}_{22}$  are much more delocalized, which is consistent with the conclusion by Leung *et al.* stating that the absence of dangling bonds on a QD surface reduces the presence of the localized in-gap states.<sup>45</sup> For better quantification of localization and the comparison between structures, we used the inverse participation ratio (IPR). This dimensionless quantity varies from 0 to 1 with limiting values corresponding to fully delocalized (0) or localized (1) Kohn-Sham wavefunction on one atom (see Computational methods for definition). The IPR values of the first four orbitals at the valence and conduction band edges for all systems under investigation are given in Table 2. The orbitals highlighted in bold corresponding to the H- and Na-ligated system are highly localized, much higher than those of K-ligated QD. This underpins the influence of ligand size and coordination on the electronic structure of non-stoichiometric QDs. Our findings that the passivation of

surface Se plays an important role in the removal of surface trap states are in line with the experimental work by Jasieniak *et al.* in which Se-rich QD is passivated with trioctylphosphine (TOP) ligand.<sup>20</sup> On the contrary, in Cd-rich QDs, most of the Se atoms are within the core and fully coordinated. Therefore, no trap states near the VB edge are observed irrespective of the ligand, with the related IPR values being slightly smaller than stoichiometric QD. Overall, in all QDs, the IPR of orbitals close to the VB edge (HOMO-3 to HOMO) indicates higher localization than that of orbitals near the CB edge (LUMO to LUMO+3). This is because the VB is localized predominantly on only Se atomic orbitals, while CB is delocalized over both Cd and Se atomic orbitals, as also shown in charge density plots (Fig. S6†).

The non-radiative excitation dynamics is guided by the interaction between electronic and vibrational subsystems. This interaction results in elastic and inelastic electron-phonon scattering. Elastic scattering is characterized by the pure-dephasing time, and it has no direct effect on energy dissipation. Inelastic scattering causes energy exchange between



**Table 2** The inverse participation ratio (IPR) for the first four orbitals at VB and CB edges in stoichiometric Cd<sub>33</sub>Se<sub>33</sub>, Cd-rich Cd<sub>28</sub>Se<sub>17</sub>X<sub>22</sub> (X = F, Cl), and three Se-rich Cd<sub>17</sub>Se<sub>28</sub>M<sub>22</sub> (M = H, Na, K) quantum dots. Large IPR values correspond to highly localized orbitals whereas small IPR values point to orbital delocalization

	Cd rich			Se rich		
	Cd <sub>33</sub> Se <sub>33</sub>	Cd <sub>28</sub> Se <sub>17</sub> F <sub>22</sub>	Cd <sub>28</sub> Se <sub>17</sub> Cl <sub>22</sub>	Cd <sub>17</sub> Se <sub>28</sub> H <sub>22</sub>	Cd <sub>17</sub> Se <sub>28</sub> Na <sub>22</sub>	Cd <sub>17</sub> Se <sub>28</sub> K <sub>22</sub>
HOMO−3	0.10	0.11	0.07	0.09	0.09	0.05
HOMO−2	0.11	0.07	0.06	<b>0.16</b>	<b>0.17</b>	0.06
HOMO−1	0.09	0.10	0.07	<b>0.54</b>	<b>0.12</b>	0.09
HOMO	0.09	0.09	0.05	<b>0.18</b>	<b>0.16</b>	0.08
LUMO	0.03	0.02	0.02	0.03	0.02	0.02
LUMO+1	0.05	0.03	0.03	0.05	0.03	0.03
LUMO+2	0.03	0.04	0.03	0.10	0.03	0.04
LUMO+3	0.03	0.03	0.02	0.04	0.04	0.03

electrons and phonons and it is characterized by non-adiabatic coupling (NAC). The frequency of the charge transition between two electronic states is directly proportional to the NAC between them. Fig. 3 shows the average coupling strength between consecutive orbitals that are involved in electron relaxation starting from 1 eV in the CB to the band edge. The coupling strength between LUMO and LUMO+1 is crucial from the dynamics viewpoint as discussed later and hence it is shown as a separate bar plot in blue. The NAC values are shown only between the consecutive orbitals as it is being the dominating factor that drives most of the energy dissipation. When two states differ by two or more orbitals, the coupling between them is weak (Fig. S7<sup>†</sup>), indicating that the transition across large energy gaps is less likely.

The magnitude of NAC between the first two orbitals of CB is quite low due to the large energy difference, since NAC is

inversely proportional to the energy gap,  $\epsilon_k - \epsilon_j$ , between the two electronic states  $k$  and  $j$ , as shown in eqn (1) in Computational methods. NAC is also directly proportional to the nuclear velocity  $\dot{R}$ , and the nuclear velocities are inversely proportional to the atomic mass at a given temperature. H is the lightest of all the ligands, thus dramatically increasing the NAC for H-ligated QDs – at least three times compared to other QDs. For similar reasons, F-ligated QD has a larger magnitude of NAC between consecutive orbitals compared to the Cl-ligated Cd-rich QD system. The H- and F-ligated systems also have the largest NAC between LUMO and (LUMO+1). In contrast, the NAC values for Na- and K-ligated systems do not show a large difference, with NAC value in the Na-ligated system being only slightly larger than that in the K-ligated system, as expected from eqn (1). The largest values of NAC of the H- and F-ligated QDs associated with large nuclear velocities may result in breaking of some bonds in the system during dynamical processes. This might lead to ligand detachment from the QD surface and the overall instability and rearrangement of the system. To check stability of considered systems, we compared the radial distribution function  $g(r)$  for Cd–Se bonds and Cd(Se)–ligand bonds in static initial structures with those averaged over 5 picoseconds of AIMD trajectory (Fig. S8<sup>†</sup>). Insignificant deviations between the static and time-averaged  $g(r)$  point to the stability of all nanostructures with no ligands breaking their bonds with the surface during electron relaxation dynamics.

The calculated time evolution of non-radiative phonon-mediated electron relaxation energy for Cd-rich and Se-rich non-stoichiometric quantum dots is shown in Fig. 4a and b, respectively. The corresponding population evolution is shown in Fig. S9<sup>†</sup>. The initially excited state electron and hole charge densities are dominated by Cd(Se) atomic orbitals, with little contribution from the ligands (Fig. S10<sup>†</sup>). The orbital for initial excitation is chosen at 1 eV above the LUMO. Observed dynamics of electrons suggests two distinct rates: (i) a major part of relaxation from the initially excited state to the second lowest unoccupied orbital (LUMO+1) takes place within a few picoseconds through the dense manifold of electronic states; (ii) relaxation from (LUMO+1) to the band edge takes hundreds of picoseconds. The fast component is highlighted by enlarging the initial dynamics for 15 ps, as shown in the insets of Fig. 4a

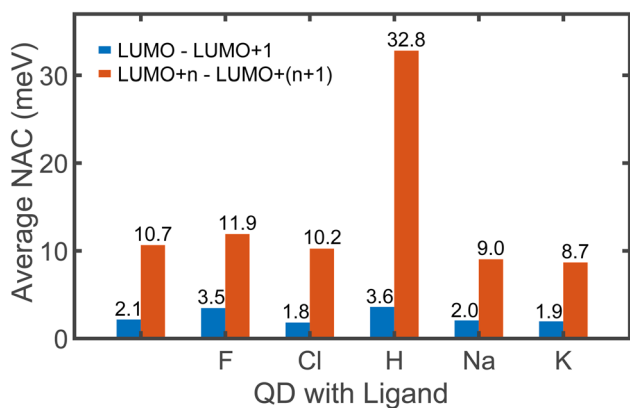


**Fig. 3** The average non-adiabatic coupling (NAC) between the Kohn–Sham orbitals involved in electron relaxation. The LUMO is always separated from the rest of the conduction band by an energy greater than 0.4 eV. Consequently, the NAC between LUMO and (LUMO+1) is weak and is considered separately, as shown in blue. The average coupling between consecutive orbitals of higher energy, *i.e.*, (LUMO +  $n$ ) and (LUMO +  $n$  + 1) is shown in orange. Here,  $n$  is an integer greater than 0. The number of orbitals considered in the range is different for all QDs, as we include just the orbitals within 1 eV of the CB. We do not consider the coupling between non-consecutive orbitals due to its negligible magnitude, as shown in Fig. S7<sup>†</sup>.



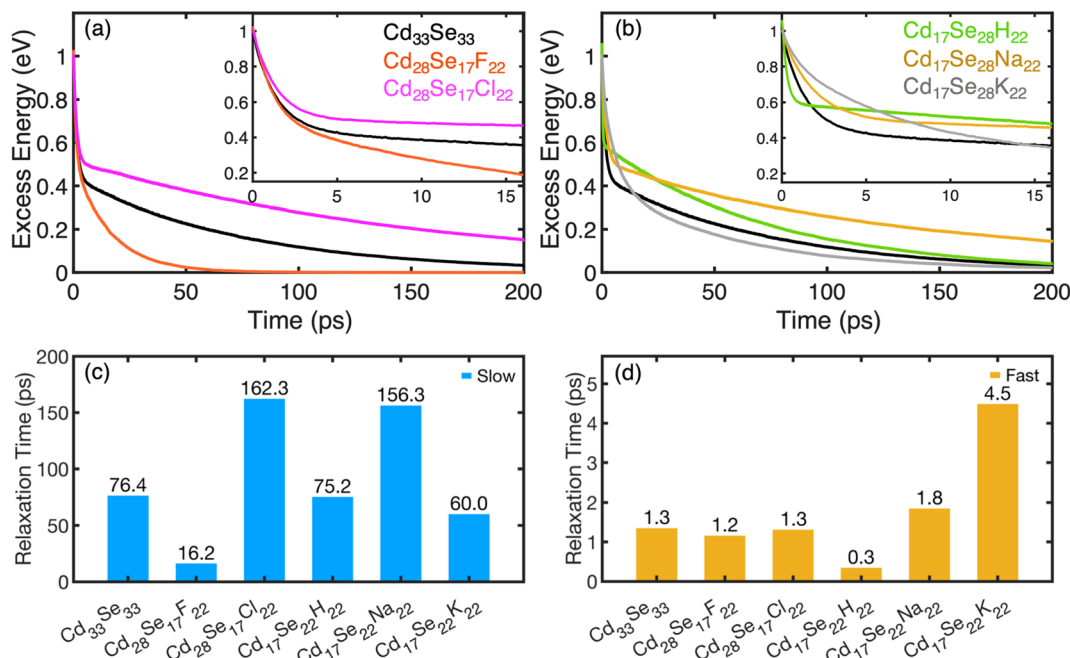


Fig. 4 The excess energy dissipation over time during electron relaxation in Cd-rich QDs (a) and in Se-rich QDs (b). The electron relaxation in QDs demonstrates two distinct rate components (fast and slow). Insets show the zoomed-in plots for the decay of the fast component. The curves fit a biexponential function given by eqn (2) with the relaxation time components  $\tau_1$  (slow) and  $\tau_2$  (fast) for all systems under study compared in (c) and (d), respectively. Table S6 in the ESI† compares the relaxation time components.

and b. The frequencies of phonons strongly coupled to the initial and the final electron/hole states are shown in Fig. S11.† The QDs containing smaller ligands have significant contributions of higher frequency vibrations ( $>300\text{ cm}^{-1}$  in Se-rich and  $>500\text{ cm}^{-1}$  in Cd-rich). Thus, we can conclude that the ligands control the lattice vibrations.

The maximum phonon frequency contributing to NAC does not exceed  $800\text{ cm}^{-1}$  for all nanostructures, which corresponds to  $\sim 0.1\text{ eV}$ , compared to the energy gap of at least  $0.4\text{ eV}$  between the first and second lowest unoccupied orbitals. This mismatch leads to a “phonon bottleneck”, which takes place when the energy difference between the electronic states is greater than the participating phonon frequencies. This consequently accounts for the slow dynamical component. As such, the dynamics rates are quantified by fitting the energy decay plots to a bi-exponential function.

$$E(t) = ae^{-\frac{t}{\tau_1}} + (1-a)e^{-\frac{t}{\tau_2}}$$

where  $\tau_1$  and  $\tau_2$  are the slow and fast time components, respectively. Fig. 4c and d show bar graphs that compare these components between analyzed QDs. The  $\tau_1$  represents the slow component of dynamics, and it has relevance only to the two lowest unoccupied KS orbitals. This component solely demonstrates the phonon bottleneck – otherwise, electron relaxation would happen on a scale of a few picoseconds. In general, the charge relaxation depends on three major factors: (i) energy gap, (ii) NAC magnitude, and (iii) pure-dephasing time. Notable, for F-ligated QD, the slow component of relaxation is fast, *i.e.*, it displays negligible bottleneck. This can be attributed to two

predominant factors: (i) large NAC values between the relevant electronic states due to the small size of F, (ii) small energy gap between LUMO and (LUMO+1). Furthermore, the large root-mean-square (RMS) value of NAC suggests large fluctuations, as shown in Table S5.† At time steps, when NAC is large, the dynamics is accelerated, and we overall see a fast rate. The same magnitude of NAC in the H-ligated system is overcompensated by its large energy gap, resulting in a longer “slow” component of electron relaxation time. In others, *i.e.*, Cl-, Na-, and K-ligated QDs, the NAC magnitude between LUMO and LUMO+1 is approximately half as that of H- and F-ligated QDs. Additionally, the corresponding energy gap in Cl- and Na-ligated systems is similar, compared to much smaller energy gap in K-ligated QD (Fig. S5†). Consequently, the electron relaxation dynamics displays maximum bottleneck in Cl- and Na-ligated QDs, and, K-ligated QD has a relatively fast “slow” component of electron relaxation time. Worth noting that F<sup>-</sup> and Cl<sup>-</sup> ligands in Cd-rich QDs are only slightly larger in size compared to Na<sup>+</sup> and K<sup>+</sup>, respectively, in Se-rich QDs. However, the structural dynamics is controlled by several factors, rather than only the ion size, and there is no straightforward rule that governs it all. The “fast” component of the electron dynamics for Se-rich QDs is the fastest for H-ligated and the slowest for the K-ligated system. This can be rationalized by a larger NAC value and smaller energy differences between consecutive orbitals for small ligands. Cd-rich QDs display rates similar to those of their stoichiometric counterparts. To find the dependence of the relaxation pathway on the initial excited state, we perform dynamics simulations starting at  $1.5\text{ eV}$  above the LUMO and



from (LUMO+1) to the LUMO as shown in Fig. S12.† The trend for the energy evolution stays the same as in the 1 eV case.

Relative to electrons, the hole relaxation is about a hundred times faster, as it happens through a dense manifold of states (Fig. S13†). To investigate the decoherence effect, we compared hole relaxation starting at 1 eV and 1.5 eV from the VB edge using the FSSH method, which doesn't account for decoherence effects, and the DISH algorithm, which includes decoherence correction. Despite an order of magnitude faster relaxation time for FSSH data compared to DISH, both methods show similar trends in hole relaxation for QDs with heavy ligands. However, systems with  $F^-$  and  $H^+$  ligands feature more significant deviations between methods due to the presence of small sub-gaps at the VB near its edge (Fig. S5†), resulting in a shorter dephasing time than the quantum transition time. Overall, inclusion of the decoherence effect in NAMD is important even for relatively dense states of heavy holes. However, regardless of the method used, though, non-stoichiometry makes the holes decay faster as a result of stronger NACs originates from surface-ligand states.

## Conclusion

In summary, we study the exciton relaxation dynamics of non-stoichiometric quantum dots with cation-rich and anion-rich surfaces. Different charge-neutralizing ligands –  $F^-$  and  $Cl^-$  ligands in cation-rich and  $H^+$ ,  $Na^+$  and  $K^+$  ligands in anion-rich QDs – are used to passivate the surfaces. We find the presence of highly localized trap states at the VB edge of anion-rich QDs as a result of the undercoordination of surface Se atoms. Noteworthy, the trap states disappear upon using bulkier ligand  $K^+$ . In addition, such trap states are absent from cation-rich counterparts because of the limited exposure of Se atoms on the surface. Depending on the size and coordination of the ligand, we observe the different electronic structures and electron-phonon coupling strengths, which leads to different non-radiative rates of phonon-mediated relaxation of the electron. The slowdown of the relaxation rate would potentially increase the efficiency of hot carrier transport and emphasize the dynamics of charges governed by many-body electronic interactions. This underpins the importance of ligand engineering in non-stoichiometric nanocrystals for different applications. Our study guides future work to Taylor QD-based materials for various applications through a strategic synthesis process.

## Computational methods

TD-DFT calculations in Kohn Sham (KS) framework<sup>46,47</sup> were performed using the Vienna *Ab initio* Simulation Package (VASP)<sup>48–50</sup> which uses a converged plane-wave basis with a cutoff of 550 eV. VESTA software is used as a visualization tool.<sup>51</sup> The Perdew–Burke–Ernzerhof (PBE) functional was used to calculate the exchange-correlation effects.<sup>52</sup> The PBE functional is well known to underestimate the band gaps due to self-interaction errors.<sup>53</sup> Hybrid functionals include exact Hartree–Fock exchange and are known to reproduce the experimental band gaps.<sup>54</sup> However, these methods require additional

computational efforts, which are expensive for NAMD, and our current calculations involve only the intraband charge relaxation. Additional calculations with the inclusion of spin–orbit coupling were done for all QDs and it is realized that SOC does not affect the electronic structure considerably (see Fig. S3 and Table S3 in ESI†). The interactions between ionic cores and valence electrons are described using the projector augmented wave (PAW)<sup>55</sup> method with 4d and 5s (Cd), 4s and 4p (Se), 2s and 2p (F), 3s and 3p (Cl), 1s (H), 3s (Na) and 3s, 3p and 4s (K) electrons treated as valence electrons. The cubic simulation cell containing QD was repeated in three dimensions and to avoid spurious interactions with its replica, a vacuum of at least 10 Å was placed in all directions. The smallest distance between a QD and its replica in *x*, *y*, and *z* directions is listed in Table S1.† To verify if the vacuum space is sufficient to avoid interactions between a quantum dot and its image, we increased the lattice vector length of the cubic unit cell by 8 Å and 16 Å in all three directions and compared the electronic structure of systems with varied cubic simulation cell dimensions (Fig. S1†). For comparison, we plot PDOS (Fig. S2†), band gaps and projection of HOMO and LUMO over the Cd, Se, and ligand atomic orbitals (Table S2†). All structures were completely optimized until the interatomic energy and forces are less than  $10^{-6}$  eV and  $10^{-3}$  eV Å<sup>-1</sup>, respectively. The AIMD simulations use these optimized structures as the initial geometries and gradually heat up those to 300 K through repeated velocity rescaling in 2 ps. Furthermore, the equilibration process was conducted at 300 K using the canonical ensemble (NVT). Finally, 5 ps adiabatic MD trajectories were generated in the microcanonical ensemble (NVE) at one femtosecond time step for each cluster.

Non-adiabatic coupling (NAC) matrix elements are computed for the relevant electronic states along the 5 ps trajectory at each time step using the CA-NAC package.<sup>56</sup> Mathematically, time-dependent NAC matrix element  $d_{jk}\dot{R}$  between states *j* and *k* is defined as:

$$d_{jk}\dot{R} = \langle \phi_j | \nabla_R | \phi_k \rangle \frac{dR}{dt} = \frac{\dot{R}}{\varepsilon_k - \varepsilon_j} \left\langle \phi_j \left| \frac{\partial \hat{H}}{\partial R} \right| \phi_k \right\rangle \quad (1)$$

Here  $\phi_j$ ,  $\phi_k$ ,  $\varepsilon_j$  and  $\varepsilon_k$  are the wave functions and energies of electronic states *j* and *k*,  $\hat{H}$  is the electronic Hamiltonian and  $\dot{R}$  is the velocity of the nuclei. NAC for two electronic states governs the charge transfer between them, and it depends on (i) the energy gap  $\varepsilon_k - \varepsilon_j$ , (ii) electron–phonon coupling matrix elements,  $\langle \phi_j | \frac{\partial \hat{H}}{\partial R} | \phi_k \rangle$  and (iii) the nuclear velocity  $\dot{R}$ . To simulate the charge relaxation dynamics on the timescale of hundreds of picoseconds, the 5 ps Hamiltonian is repeated several times. The *ab initio* dynamics timescale is long enough to capture the statistical vibrational information at the raised temperature (Fig. S4†).

The energy of each Kohn–Sham orbital and the coupling between them were fed into the quantum-classical DISH technique. DISH is useful when the pure dephasing time is shorter than the quantum transition time.<sup>57</sup> In QDs, since the electronic states near the conduction band edge are discrete and have



considerable energy differences, decoherence effects are important.<sup>58</sup> DISH follows the classical path approximation (CPA), as it is implemented within the real-time TD-DFT framework in the Python eXtension for *Ab Initio* Dynamics (PYXAID) package.<sup>59,60</sup> DISH method incorporates the decoherence effects which are otherwise missing in the commonly used Fewest Switch Surface Hopping (FSSH).<sup>61</sup> DISH slows down the dynamics compared to FSSH as exemplified by the quantum Zeno effect.<sup>35</sup> A semiclassical estimate of the quantum decoherence time is calculated using the pure dephasing function of the optical response theory. To estimate the decoherence effects, hole relaxation dynamics using the FSSH approach are also performed (Fig. S13<sup>†</sup>), showing an order of magnitude faster relaxation time compared to those obtained by DISH methods. For reliable results, we average 10 000 electron–nuclear evolutions modeled by using 100 initial conditions and 100 stochastic hop sequences per initial condition. The DISH approach has been applied to study the photoinduced exciton dynamics in a broad set of nanomaterials in the literature.<sup>62–68</sup> A detailed description of the methodology adopted in this study can be found elsewhere.<sup>69</sup>

Inverse participation ratio (IPR) corresponding to the *i*th KS state is calculated as:

$$\text{IPR}_i = \frac{\sum_{\alpha} |c_{\alpha,i}|^4}{\left(\sum_{\alpha} |c_{\alpha,i}|^2\right)^2} \quad (2)$$

where  $\alpha$  is the index of summation, from 1 to  $n_{\text{atoms}}$ . Here  $n_{\text{atoms}}$  is equal to the number of atoms in the cluster.  $|c_{\alpha,i}|^2$  represents the magnitude of projection of *i*th KS state over  $\alpha$  atomic orbital. Typically, if a particle is localized on only one atomic orbital IPR is equal to 1, while IPR tends to 0 for the highly delocalized KS states. In VASP, the Kohn–Sham wavefunctions  $\phi_{ni}$  corresponding to (*n*th *k*-point, *i*th band) pair are projected onto spherical harmonics around each ion to calculate the site projected wave function  $|\langle Y_{lm}^{\alpha} | \phi_{ni} \rangle|^2$ . Here  $Y_{lm}^{\alpha}$  is the spherical harmonic centered at  $\alpha$ -th ion, where *l* and *m* represent the angular momentum and magnetic quantum numbers. Only spherical harmonics that are non-zero within spheres of a Wigner–Seitz radius around each ion are considered.  $|c_{\alpha,i}|^2$  is calculated by summing all the site projected wavefunctions around  $\alpha$ -th ion for *k*-point  $n = 1$ ,

$$|c_{\alpha,i}|^2 = \sum_{l,m} |\langle Y_{lm}^{\alpha} | \phi_{1i} \rangle|^2 \quad (3)$$

## Conflicts of interest

There are no conflicts to declare.

## Acknowledgements

The work at Los Alamos National Laboratory (LANL) was supported by the Laboratory Directed Research and Development (LDRD) programme at LANL under project 20200213DR. This

work was done in part at the Center for Nonlinear Studies (CNLS) and the Center for Integrated Nanotechnologies (CINT), a U.S. Department of Energy and Office of Basic Energy Sciences user facility, at LANL. This research used resources provided by the LANL Institutional Computing Program. Los Alamos National Laboratory is operated by Triad National Security, LLC, for the National Nuclear Security Administration of the U.S. Department of Energy (Contract No. 89233218NCA000001). O. V. P. acknowledges support of the US Department of Energy, grant No. DE-SC0014429. S. K. acknowledges support of the National Science Foundation under grant No. 2004197. For computational resources, the authors acknowledge the Center for Computationally Assisted Science and Technology (CCAST) at North Dakota State University and the National Energy Research Scientific Computing Center (NERSC), supported by the Office of Science of the Department of Energy under Contract DE-AC02-439 05CH11231. All authors thank Dr Victor I. Klimov for fruitful discussions. DG acknowledges the IIT Delhi SEED Grant (PLN12/04MS), the Science and Engineering Research Board (SERB), Department of Science and Technology (DST), India for Start-up Research Grant SRG/2022/001234 and the IIT Delhi HPC facility for computational resources.

## References

- 1 M. G. Bawendi, M. L. Steigerwald and L. E. Brus, *Annu. Rev. Phys. Chem.*, 1990, **41**, 477–496.
- 2 S. V. Gaponenko, *Optical Properties of Semiconductor Nanocrystals*, Cambridge University Press, Cambridge, 1998.
- 3 A. Foerster and N. A. Besley, *J. Phys. Chem. A*, 2022, **126**, 2899–2908.
- 4 M. A. Cotta, *ACS Appl. Nano Mater.*, 2020, **3**, 4920–4924.
- 5 D. Harankahage, J. Cassidy, M. Yang, D. Porotnikov, M. Williams, N. Kholmicheva and M. Zamkov, *J. Phys. Chem. C*, 2021, **125**, 22195–22203.
- 6 D. Ghosh, S. A. Ivanov and S. Tretiak, *Chem. Mater.*, 2021, **33**, 7848–7857.
- 7 S. Kilina, S. Ivanov and S. Tretiak, *J. Am. Chem. Soc.*, 2009, **131**, 7717–7726.
- 8 S. Kilina, K. A. Velizhanin, S. Ivanov, O. V. Prezhdo and S. Tretiak, *ACS Nano*, 2012, **6**, 6515–6524.
- 9 S. V. Kilina, P. K. Tamukong and D. S. Kilin, *Acc. Chem. Res.*, 2016, **49**, 2127–2135.
- 10 N. A. Hill and K. B. Whaley, *J. Chem. Phys.*, 1994, **100**, 2831–2837.
- 11 K. L. Sowers, Z. Hou, J. J. Peterson, B. Swartz, S. Pal, O. Prezhdo and T. D. Krauss, *Chem. Phys.*, 2016, **471**, 24–31.
- 12 E. A. Weiss, *Acc. Chem. Res.*, 2013, **46**, 2607–2615.
- 13 P. Guyot-Sionnest, M. Shim, C. Matranga and M. Hines, *Phys. Rev. B: Condens. Matter Mater. Phys.*, 1999, **60**, R2181–R2184.
- 14 P. Guyot-Sionnest, B. Wehrenberg and D. Yu, *J. Chem. Phys.*, 2005, **123**, 074709.
- 15 A. Franceschetti and A. Zunger, *Phys. Rev. B: Condens. Matter Mater. Phys.*, 2000, **62**, R16287–R16290.
- 16 M. Califano, A. Franceschetti and A. Zunger, *Nano Lett.*, 2005, **5**, 2360–2364.





- 17 A. Puzder, A. J. Williamson, F. Gygi and G. Galli, *Phys. Rev. Lett.*, 2004, **92**, 217401.
- 18 M. Yu, G. W. Fernando, R. Li, F. Papadimitrakopoulos, N. Shi and R. Ramprasad, *Appl. Phys. Lett.*, 2006, **88**, 231910.
- 19 A. J. Houtepen, Z. Hens, J. S. Owen and I. Infante, *Chem. Mater.*, 2017, **29**, 752–761.
- 20 J. Jasieniak and P. Mulvaney, *J. Am. Chem. Soc.*, 2007, **129**, 2841–2848.
- 21 H. H. Wei, C. M. Evans, B. D. Swartz, A. J. Neukirch, J. Young, O. V. Prezhdo and T. D. Krauss, *Nano Lett.*, 2012, **12**, 4465–4471.
- 22 W. Xia, J. Wu, J. C. Hu, S. Sun, M. D. Li, H. Liu, M. Lan and F. Wang, *ChemSusChem*, 2019, **12**, 4617–4622.
- 23 M.-Y. Huang, X.-B. Li, Y.-J. Gao, J. Li, H.-L. Wu, L.-P. Zhang, C.-H. Tung and L.-Z. Wu, *J. Mater. Chem. A*, 2018, **6**, 6015–6021.
- 24 M. Bhati, S. A. Ivanov, T. P. Senftle, S. Tretiak and D. Ghosh, *J. Mater. Chem. A*, 2022, **10**, 5212–5220.
- 25 T. F. Lu, S. Gumber, M. V. Tokina, J. A. Tomko, P. E. Hopkins and O. V. Prezhdo, *Nanoscale*, 2022, **14**, 10514–10523.
- 26 W. A. Tisdale, K. J. Williams, B. A. Timp, D. J. Norris, E. S. Aydil and X. Y. Zhu, *Science*, 2010, **328**, 1543–1547.
- 27 Y. Gao and X. Peng, *J. Am. Chem. Soc.*, 2015, **137**, 4230–4235.
- 28 O. V. Prezhdo, *Chem. Phys. Lett.*, 2008, **460**, 1–9.
- 29 P. T. Landsberg, *Recombination in Semiconductors*, Cambridge University Press, Cambridge, 1992.
- 30 X.-Q. Li, H. Nakayama and Y. Arakawa, *Phys. Rev. B: Condens. Matter Mater. Phys.*, 1999, **59**, 5069–5073.
- 31 T. Inoshita and H. Sakaki, *Phys. B*, 1996, **227**, 373–377.
- 32 S. V. Kilina, D. S. Kilin and O. V. Prezhdo, *ACS Nano*, 2009, **3**, 93–99.
- 33 G. Zhou, G. Lu and O. V. Prezhdo, *Nano Lett.*, 2021, **21**, 756–761.
- 34 D. J. Trivedi, L. Wang and O. V. Prezhdo, *Nano Lett.*, 2015, **15**, 2086–2091.
- 35 S. V. Kilina, A. J. Neukirch, B. F. Habenicht, D. S. Kilin and O. V. Prezhdo, *Phys. Rev. Lett.*, 2013, **110**, 180404.
- 36 A. Pandey and P. Guyot-Sionnest, *Science*, 2008, **322**, 929–932.
- 37 R. D. Schaller, V. M. Agranovich and V. I. Klimov, *Nat. Phys.*, 2005, **1**, 189–194.
- 38 J. Huang, Z. Huang, Y. Yang, H. Zhu and T. Lian, *J. Am. Chem. Soc.*, 2010, **132**, 4858–4864.
- 39 A. J. Nozik, *Phys. E*, 2002, **14**, 115–120.
- 40 E. Runge and E. K. U. Gross, *Phys. Rev. Lett.*, 1984, **52**, 997–1000.
- 41 J. C. Tully, *J. Chem. Phys.*, 1990, **93**, 1061–1071.
- 42 M. D. Peterson, L. C. Cass, R. D. Harris, K. Edme, K. Sung and E. A. Weiss, *Annu. Rev. Phys. Chem.*, 2014, **65**, 317–339.
- 43 V. N. Soloviev, A. Eichhofer, D. Fenske and U. Banin, *J. Am. Chem. Soc.*, 2001, **123**, 2354–2364.
- 44 A. J. Nozik, *Annu. Rev. Phys. Chem.*, 2001, **52**, 193–231.
- 45 K. Leung and K. B. Whaley, *J. Chem. Phys.*, 1999, **110**, 11012–11022.
- 46 C. F. Craig, W. R. Duncan and O. V. Prezhdo, *Phys. Rev. Lett.*, 2005, **95**, 163001.
- 47 S. A. Fischer, B. F. Habenicht, A. B. Madrid, W. R. Duncan and O. V. Prezhdo, *J. Chem. Phys.*, 2011, **134**, 024102.
- 48 G. Kresse and J. Furthmüller, *Phys. Rev. B: Condens. Matter Mater. Phys.*, 1996, **54**, 11169–11186.
- 49 G. Kresse and J. Hafner, *Phys. Rev. B: Condens. Matter Mater. Phys.*, 1993, **47**, 558–561.
- 50 G. Kresse and J. Hafner, *Phys. Rev. B: Condens. Matter Mater. Phys.*, 1994, **49**, 14251–14269.
- 51 K. Momma and F. Izumi, *J. Appl. Crystallogr.*, 2008, **41**, 653–658.
- 52 J. P. Perdew, K. Burke and M. Ernzerhof, *Phys. Rev. Lett.*, 1996, **77**, 3865–3868.
- 53 J. P. Perdew, in *Advances in Quantum Chemistry*, ed. P.-O. Löwdin, Academic Press, 1990, vol. 21, pp. 113–134.
- 54 S. Tretiak, K. Igumenshchev and V. Chernyak, *Phys. Rev. B: Condens. Matter Mater. Phys.*, 2005, **71**, 033201.
- 55 G. Kresse and D. Joubert, *Phys. Rev. B: Condens. Matter Mater. Phys.*, 1999, **59**, 1758–1775.
- 56 W. Chu, Q. Zheng, A. V. Akimov, J. Zhao, W. A. Saidi and O. V. Prezhdo, *J. Phys. Chem. Lett.*, 2020, **11**, 10073–10080.
- 57 O. V. Prezhdo and P. J. Rossky, *J. Chem. Phys.*, 1997, **107**, 5863–5878.
- 58 J. C. Wong, L. Li and Y. Kanai, *J. Phys. Chem. C*, 2018, **122**, 29526–29536.
- 59 A. V. Akimov and O. V. Prezhdo, *J. Chem. Theory Comput.*, 2013, **9**, 4959–4972.
- 60 A. V. Akimov and O. V. Prezhdo, *J. Chem. Theory Comput.*, 2014, **10**, 789–804.
- 61 H. M. Jaeger, S. Fischer and O. V. Prezhdo, *J. Chem. Phys.*, 2012, **137**, 22A545.
- 62 S. Agrawal, W. Lin, O. V. Prezhdo and D. J. Trivedi, *J. Chem. Phys.*, 2020, **153**, 054701.
- 63 S. Agrawal, A. S. Vasenko, D. J. Trivedi and O. V. Prezhdo, *J. Chem. Phys.*, 2022, **156**, 094702.
- 64 C. M. Perez, D. Ghosh, O. Prezhdo, W. Nie, S. Tretiak and A. Neukirch, *J. Phys. Chem. Lett.*, 2022, 5213–5219, DOI: [10.1021/acs.jpcllett.2c00575](https://doi.org/10.1021/acs.jpcllett.2c00575).
- 65 C. M. Perez, D. Ghosh, O. Prezhdo, S. Tretiak and A. J. Neukirch, *J. Phys. Chem. Lett.*, 2021, **12**, 1005–1011.
- 66 J. He, W. H. Fang, R. Long and O. V. Prezhdo, *J. Am. Chem. Soc.*, 2020, **142**, 14664–14673.
- 67 W. Li, R. Long, J. Tang and O. V. Prezhdo, *J. Phys. Chem. Lett.*, 2019, **10**, 3788–3804.
- 68 D. Ghosh, C. M. Perez, O. Prezhdo, W. Nie, S. Tretiak and A. J. Neukirch, *J. Mater. Chem. C*, 2022, **10**, 9563–9572.
- 69 S. Gumber, S. Agrawal and O. V. Prezhdo, *J. Phys. Chem. Lett.*, 2022, **13**, 1033–1041.

